A new Rossby wave model for steric sea level variability

Peter Kowalski[a,*], Arnaud Czaja[b]

[a]*Department of Physics, Imperial College, London, UK*
[b]*Department of Physics and Grantham Institute for Climate Change, Imperial College, London, UK*

Abstract

In this paper we present a new linear baroclinic Rossby wave model for steric sea surface height (SSH) fluctuations. In this model, Rossby waves are forced by variations in meridional upper ocean mass transport due to thermal wind, diffusive and lateral fluxes of buoyancy, in addition to surface wind and buoyancy forcings. We test the capacity of the new model at capturing interannual-to-decadal steric SSH variations in the North Atlantic via sensitivity experiments. The two main results of this paper are: 1) The model-simulated steric SSH derived from the new Rossby wave model is a much better match to the observed steric SSH than that of existing Rossby wave models; and 2) In the entire tropical-to-subtropical North Atlantic the model-simulated steric SSH derived from the new Rossby wave model captures 80-100% of both the phase and amplitude of low frequency steric SSH variations.

Keywords: Sea surface height, Rossby waves, Pycnocline depth.

1. Introduction

In the Atlantic and Pacific Oceans, variations in sea surface height (SSH) have been shown to be primarily due to variations in steric SSH (e.g. Polkova et al., 2015; Piecuch and Ponte 2011; Piecuch and Ponte 2012b, 2012a). In the literature, there are thus a plethora of studies that have linked the variability of the steric SSH in the Atlantic and Pacific Oceans to wind-forced baroclinic Rossby waves. [e.g. North Atlantic (Sturges et al., 1998; Cabanes et al., 2006; Zhang and Wu, 2010; Polkova et al., 2015; Zhang et al., 2016; M.Calafat et al., 2018); tropical South Atlantic (Piecuch and Ponte, 2012b);

*Corresponding author
Email address: p.kowalski@imperial.ac.uk (Peter Kowalski)

North Pacific (Capotondi and Alexander, 2001; Fu and Qiu, 2002); South Pacific (Qiu and Chen, 2006)]. In addition to these Rossby waves, Piecuch and Ponte [2012b, 2012a] have also shown that in the tropical South Atlantic and tropical Southwest Pacific baroclinic Rossby waves forced by surface buoyancy fluxes make a significant contribution to the variance of the steric SSH, but their effect on the steric SSH in other regions of the Atlantic and Pacific Oceans is yet to be explored.

The most widely used wind-driven Rossby wave model of the steric SSH in the literature is that which is derived from the 1.5 layer ocean model (e.g. Huang, 2012). In this model framework the density is crudely modelled as two layers of constant density with the interface between the two layers taken to represent the depth of the pycnocline, which is the depth in the permanent pycnocline at which the vertical density gradient is a local maximum (e.g. Feucher et al., 2016); Furthermore, the ocean dynamics are governed by the upper ocean linear vorticity balance in a wind-driven ocean that is in geostrophic and hydrostatic balance, but with only the layer above the pycnocline depth in motion. As a result, the effect of wind-stress is communicated to the pycnocline depth via Ekman pumping, and changes in the steric SSH are found to be directly proportional to those of the pycnocline depth displacement. These together lead to steric SSH anomalies that propagate westward as wind-driven baroclinic Rossby waves. However, this linear relationship between the steric SSH and the pycnocline depth displacement, which is fundamental to the derivation of the wind-driven Rossby wave model in this configuration, does not hold in the real world oceans. Indeed there are other factors particularly in the upper ocean, such as the temperature in the mixed layer(e.g. Polkova et al., 2015), that have been shown to influence the steric SSH and furthermore, these factors may also generate variability in the permanent pycnocline. With this in mind, in this paper we develop a new ocean model framework in which, as in the 1.5 layer model, the ocean dynamics are governed by the upper ocean linear vorticity balance in a wind-driven ocean that is in geostrophic and hydrostatic balance. We find that changes in steric SSH are due to both changes in vertically integrated upper ocean density and to changes in the depth of the pycnocline, the latter of which is found to be driven by both local Ekman pumping and

vertically integrated zonal and temporal density variations. As a result, we obtain a new baroclinic Rossby equation for the steric SSH in which three new baroclinic Rossby waves source terms emerge, in addition to the well established baroclinic Rossby waves forced by wind and surface buoyancy exchanges (e.g. Schneider and Miller, 2001; Piecuch and Ponte, 2012b).

This paper is organised as follows: In Section 2 we describe the data set and observed steric SSH that we use to assess the performance of the new Rossby wave model. In Section 3 we provide a description of the new model framework and derivation of the Rossby wave model. In Section 4 we test the new model by investigating its capacity to capture low-frequency variations in the North Atlantic, followed by a discussion and some suggestions for future work in Section 5.

2. Data

The data set that we use is the ECCO v4r1 ocean state estimate (Forget et al., 2016) produced by the Estimating the Circulation and Climate of the Ocean (ECCO) consortium (Wunsh and Heimbach, 2007). The data covers the period 1992-2011. Furthermore, the horizontal resolution of this particular solution in the North Atlantic is 0.25^o with 50 vertical levels of varying thickness, and the time resolution is one month. For a detailed description of the ECCO v4r1 ocean state estimate see Liang et al. [2017], who recently used this version of the solution to study bidecadal changes in ocean heat content.

At each longitude and latitude the data from ECCO v4r1 (specifically, density ρ and wind-stress) is used to derive the various forcing terms in the Rossby wave model, as well as the steric SSH η_O that is used as "observations" for comparison with the Rossby wave model steric SSH.

We form time series of anomalies for η_O and the forcing terms in the Rossby wave model by removing the time mean, linear trend and seasonal cycle. The resulting time series of anomalies for the forcing terms are then used to derive time series of model-simulated steric SSH anomalies. The time series of the model-simulated steric SSH and η_O are then low-pass filtered to remove any signals shorter than 1 year to focus on interannual-to-decadal timescales.

3. Linear oceanic model

3.1. Model framework

We consider a rectangular basin of constant depth, D, and linear perturbations about a reference state of rest. The free surface $\eta_S(x, y, t)$ is taken to be the steric SSH, which is defined as:

$$\eta_S \;=\; -\frac{1}{\rho_o}\int_{-D}^{0}(\rho-\rho_o)\,dz, \tag{1}$$

where ρ_o is a characteristic ocean density. The density ρ is decomposed as $\rho(x, y, z, t) = \hat{\rho}(z) + \rho'(x, y, z, t)$ where the hat variable refers to the reference state and the prime a small deviation from it ($\rho' \ll \hat{\rho}$).

In the classic two-layer model (e.g. Gill 1982) the density field is partitioned into two layers of constant density, say $\hat{\rho}_1$ and $\hat{\rho}_2$, to provide a model of the pycnocline as a density jump across the interface between the two layers. Denoting by H_1 the depth of the interface at rest and $\eta_1(x, y, t)$ the deviation from this position, the interface depth is $z = -H_1 - \eta_1$ [see Fig. 1(a)], so that the density field satisfies:

$$\frac{1}{H_1+\eta_1+\eta_S}\int_{-H_1-\eta_1}^{\eta_S}\rho\,dz \;\approx\; \frac{1}{H_1}\int_{-H_1}^{0}\hat{\rho}\,dz \equiv \hat{\rho}_1, \tag{2}$$

$$\frac{1}{D-H_1-\eta_1}\int_{-D}^{-H_1-\eta_1}\rho\,dz \;\approx\; \frac{1}{D-H_1}\int_{-D}^{-H_1}\hat{\rho}\,dz \equiv \hat{\rho}_2. \tag{3}$$

In our new model, we introduce, in addition to the depth H_1 of the permanent pycnocline, its thickness H_2. Following the observations by Feucher et al. (2016), we decompose further H_2 into a top and bottom thickness, i.e. $H_2 = H_T + H_B$ (note that typical values are $H_1 = 800$m, $H_T = 200$m and $H_B = 300$m, leading to $H_2 = 500$m). The pycnocline is still located at depth $z = -H_1 - \eta_1$ but we relax the condition in Eq. (2) and Eq. (3) and instead consider the average density of the top and bottom of the pycnocline layer [Fig. 1(b)]. Mathematically, this means that we replace Eq. (2) and Eq. (3) by:

$$\frac{1}{H_T+\eta_1}\int_{-H_1-\eta_1}^{-H_1+H_T}\rho\,dz \;\approx\; \frac{1}{H_T}\int_{-H_1}^{-H_1+H_T}\hat{\rho}\,dz \equiv \hat{\rho}_T, \tag{4}$$

$$\frac{1}{H_B-\eta_1}\int_{-H_1-H_B}^{-H_1-\eta_1}\rho\,dz \;\approx\; \frac{1}{H_B}\int_{-H_1-H_B}^{-H_1}\hat{\rho}\,dz \equiv \hat{\rho}_B. \tag{5}$$

With this new decomposition of the density field, the steric sea surface height in Eq. (1) can be written as:

$$\eta_S = -\left(\int_{-H_1+H_T}^{0}(\rho-\rho_o)\ dz + \int_{-D}^{-H_1-H_B}(\rho-\rho_o)\ dz + \int_{-H_1-\eta_1}^{-H_1+H_T}(\rho-\rho_o)\ dz + \int_{-H_1-H_B}^{-H_1-\eta_1}(\rho-\rho_o)\ dz\right)/\rho_o. \tag{6}$$

The first two terms on the r.h.s reflect steric height variations due to density changes above and below the pycnocline layer, respectively, while the last two reflect steric height variations due to density changes within the pycnocline. In the following, we neglect density variations below the pycnocline layer compared to those above and we take the latter as given. Under this assumption, and using Eq. (4) and Eq. (5), the time derivative of Eq. (6) is:

$$\frac{\partial \eta_S}{\partial t} \approx \left(\frac{\hat{\rho}_B - \hat{\rho}_T}{\rho_o}\right)\frac{\partial \eta_1}{\partial t} + G_{\rho_t}, \tag{7}$$

where

$$G_{\rho_t} \equiv -\frac{\partial}{\partial t}\left(\int_{-H_1+H_T}^{0}\rho\ dz\right)/\rho_o. \tag{8}$$

We show next that adding a few dynamical assumptions allow to turn this equation into a Rossby wave equation for the steric sea surface height.

3.2. Rossby wave model of the steric SSH

The wind is assumed to act in a thin Ekman layer of thickness δ_E below the sea surface. It creates fluctuations in Ekman pumping velocity W_E which drive north south flow v below the Ekman layer according to Sverdrup vorticity balance: $\beta v = f\frac{\partial w}{\partial z}$ where f is the Coriolis parameter and β its meridional gradient. Integrated vertically from the depth of the pycnocline to the base of the Ekman layer where the vertical velocity is W_E, the Sverdrup vorticity balance becomes:

$$\int_{-H_1-\eta_1}^{-\delta_E}\beta v\ dz = f(W_E + \frac{\partial \eta_1}{\partial t}). \tag{9}$$

(Note that in deriving this equation, we have treated the pycnocline as a material surface and linearised the associated boundary condition). This equation is coupled to Eq. (7) because the meridional flow

is in geostrophic balance and thus associated with a zonal pressure (and sea surface height) gradient. It is shown in Appendix A that under the assumption of geostrophy and hydrostatic balance, very thin Ekman layer and $\eta_1 \ll H_1$, the l.h.s of Eq. (9) can be rewritten as:

$$\int_{-H_1-\eta_1}^{-\delta_E} \beta v \; dz \approx \frac{\beta g}{f}\left(H_1 \frac{\partial \eta_S}{\partial x} + \int_{-H_1}^{0} [\int_z^0 \frac{\partial \rho}{\partial x} \; dz'] \; dz/\rho_o\right). \tag{10}$$

As a result, we have:

$$\frac{\beta g}{f}\left(H_1 \frac{\partial \eta_S}{\partial x} + \int_{-H_1}^{0} [\int_z^0 \frac{\partial \rho}{\partial x} \; dz'] \; dz/\rho_o\right) \approx f(W_E + \frac{\partial \eta_1}{\partial t}). \tag{11}$$

Combining this equation with Eq. (7) finally leads to a Rossby wave equation for the steric sea surface height η_S, namely:

$$\boxed{\frac{\partial \eta_S}{\partial t} + C_R \frac{\partial \eta_S}{\partial x} \;=\; -\frac{\hat{g}'}{g} W_E + G_{\rho_t} + G_{\rho_x} - \epsilon \eta_S,} \tag{12}$$

where G_{ρ_t} was introduced in Eq. (8), and where

$$G_{\rho_x} \equiv \frac{\beta \hat{g}'}{f^2} \int_{-H_1}^{0} [\int_z^0 \frac{\partial \rho}{\partial x} \; dz'] \; dz/\rho_o \tag{13}$$

represents the impact of zonal gradients of density above the depth of the pycnocline on the steric surface height (equivalent to upper ocean meridional mass transport associated with geostrophic thermal wind). In addition we have introduced the reduced gravity $\hat{g}'$ and Rossby phase speed C_R:

$$\hat{g}' \;\equiv\; \frac{g(\hat{\rho}_B - \hat{\rho}_T)}{\rho_o} \quad \text{and} \quad C_R(y) \;\equiv\; -\frac{\hat{g}' \beta H_1}{f^2} < 0. \tag{14}$$

Note that C_R depends on the thickness of the permanent pycnocline H_2 via $\hat{\rho}_T$ and $\hat{\rho}_B$ in Eq. (4) and Eq. (5). For a discussion of the response of C_R to variations in H_2 the reader is referred to Appendix B. Note also that, following the work of, for example, Zhang and Wu [2010] and Zhang et al. [2016], we have added an extra linear damping term on the r.h.s of Eq. (14), namely $-\epsilon \eta_S$, to include the effects of dissipation (e.g. destabilization of long Rossby waves by baroclinic instability –see Lacasce and Pedlosky, 2004).

Eq. (12) shows that Rossby waves are forced by local Ekman pumping W_E as well as density variations (temporal and zonal) above the permanent pycnocline layer. This contrasts with the classic

two-layer model forced by Ekman pumping only. Following Piecuch and Ponte [2011] the term due to temporal variations can be written as:

$$G_{\rho_t} \;=\; \mathcal{A} + \mathcal{D} + \mathcal{Q}, \tag{15}$$

where $\mathcal{A}$, $\mathcal{D}$ and $\mathcal{Q}$ represent fluxes of buoyancy due to advection, diffusion and surface fluxes of heat/freshwater. Their Rossby wave model forced by wind and surface buoyancy exchanges can be recovered here by setting $G_{\rho_x}, \mathcal{D}, \mathcal{A} = 0$. In our model there are therefore three new baroclinic Rossby waves sources forced by buoyancy fluxes due to advection and diffusion, and upper ocean meridional mass transport due to thermal wind (G_{ρ_x}). Note, in the analysis of the new model in the next section we do not isolate $\mathcal{A}$, $\mathcal{D}$ and $\mathcal{Q}$. This would require computing budgets of $\mathcal{A}$, $\mathcal{D}$ and $\mathcal{Q}$ (e.g. Piecuch and Ponte, 2011), which is beyond the scope of the present study.

4. Test of the new Rossby wave model in the North Atlantic from 5^{o}N to 60^{o}N

As in previous studies (e.g. Cabanes et al., 2006; Fu and Qiu, 2002), the analytical solution to Eq. (12) is obtained by integrating along Rossby wave characteristics $x - C_R t = constant$. As shown in Appendix C the general form of this solution is

$$\eta_S \;=\; \eta_B + F_{W_E} + F_{\rho_x} + F_{\rho_t}, \tag{16}$$

where F_{W_E}, F_{ρ_t} and F_{ρ_x} represent, respectively, local Ekman pumping, and temporal (F_{ρ_t}) and zonal (F_{ρ_x}) density variations integrated along Rossby wave characteristics (these latter two terms are direct functions of the G_{ρ_t} and G_{ρ_x} terms introduced earlier, see Appendix C); and η_B is the eastern boundary forcing, which is computed using the observed steric SSH η_O at the eastern boundary. In this section we investigate the capacity of the new Rossby wave model to capture low-frequency steric SSH variations in the North Atlantic via a number of sensitivity experiments using η_S in Eq. (16). To do so we use the skill metric defined as:

$$S_i \;=\; \left(1 - \frac{<(\eta_O - \eta_S)^2>}{<\eta_O^2>}\right) \times 100\%, \tag{17}$$

where i is the sensitivity experiment (e.g. $i = \eta_B$ denotes forecast skill when the model is driven by the eastern boundary forcing only), $< . >$ denotes ensemble average, and η_O and η_S are the low-pass filtered observed and model-simulated steric SSH respectively. In this formula values of S_i range from $-\infty$ to 100%. $S_i \rightarrow 100\%$ indicates that η_S is very close to η_O in both phase and amplitude while $S_i < 0$ indicates that η_S captures the phase but overestimates the magnitude of η_O. An example from the literature is in Zhang and Wu [2010] who found that correlations (phase) between model-simulated SSH anomalies derived from the linear wind-forced Rossby wave model and observed SSH can exceed 0.7 but the associated forecast skill is as low as 20% or even negative.

Briefly, we also computed correlations between η_O and η_S at each longitude and latitude for each of the sensitivity experiments. We found that the regions that yielded statistically significant correlations, which were found to be in the range $0.6 \sim 1$, were those which generally included values of S in the range $10\% \sim 100\%$. In all the figures showing S_i in this section the regions with $S_i < 10\%$ have been masked. Furthermore, as part of the analysis in this section we also investigated the effect of varying the damping rate ϵ on S_i, with values of ϵ in the range [0 (no damping) $\sim (0.01yr)^{-1}$ (strong damping)]. We found from each of the sensitivity experiments that the values of ϵ that roughly yielded the largest number of high values of forecast skill in the tropical-to-subtropical, subtropical-to-midlatitude and midlatitude-to-subpolar North Atlantic were $\epsilon \approx 0$, $\epsilon \approx (1yr)^{-1}$ and $\epsilon \approx (0.5yr)^{-1}$ respectively. All the figures showing S_i in this section have thus been computed with $\epsilon = 0$ in the tropical-to-subtropical North Atlantic, $\epsilon = (1yr)^{-1}$ in the subtropical-to-mid-latitude North Atlantic, and $\epsilon = (0.5yr)^{-1}$ in the mid-latitude-to-subpolar North Atlantic. [For a discussion of the various constants, Rossby wave phase speed used for the model integrations, methods for computing the forcing terms, and model domain for illustrating the solution in a realistic ocean the reader is referred to Appendices B and C.]

4.1. Results

4.1.1. New Rossby wave model

Fig. 2 shows the forecast skill, S_N, for the new Rossby wave model with all forcing terms in Eq. (12) included. Near the eastern boundaries the solution for η_S in Eq. (16) is dominated by η_B, which is partly determined from the observed steric SSH η_O. Thus, unsurprisingly it can be seen that near the eastern boundaries S_N is large with values in the range $80\% \sim 100\%$.

In the subpolar North Atlantic the skill of the model is generally poor, with $S_N < 10\%$ over most of the subpolar North Atlantic except for a small region at roughly $45^o\text{N} - 50^o\text{N}, 15^o\text{W} - 25^o\text{W}$ where S_N is between 30% and 70%. In the subtropical-to-midlatitude North Atlantic the skill of the model is excellent, with S_N generally between 60% and 90%, except at a few small regions (e.g. mid-Atlantic ridge) where values of S_N are in the range $20\% \sim 50\%$. Finally, in the tropical-to-subtropical North Atlantic the model is almost a perfect match to the observed, with S_N generally in the range $80\% \sim 100\%$. Note that $S_N > 90\%$ everywhere in the region enclosed by $5^o\text{N} - 15^o\text{N}$, the eastern boundaries and roughly 50^oW.

4.1.2. Sensitivity experiments

An important test of the new model is to check if S_N in Fig. 2 is larger than S_i computed when some of the forcing terms are omitted, or when some of the terms are isolated in the model (e.g. Ekman pumping only). We thus performed a variety of sensitivity experiments and found that S_i is generally much smaller than S_N in the tropical-to-mid-latitude North Atlantic, however, as in Fig. 2, S_i remains below 10% in the subpolar North Atlantic in all sensitivity experiments. Examples of S_i computed from the sensitivity experiments are shown and described in Figs. 3-5. In particular, Fig. 4(a) and Fig. 4(b) show the classical Ekman pumping solution with and without eastern boundary forcing. Comparison of these figures with the solution of the full model in Fig. 2 clearly indicates that our new Rossby wave model provides a very significant improvement towards predicting SSH variations in the North Atlantic. Fig. 5 suggests that the improvement results from the two new forcing terms

linked to temporal and zonal variations in the upper ocean density field (G_{ρ_t} and G_{ρ_x}, respectively), especially along the separated Gulf Stream [Fig. 5(a)].

In the study of Cabanes et al.[2006] eastern boundary steric SSH anomalies η_B were found to be only important near the eastern boundaries. By comparing Fig. 2 with Fig. 3(a), which shows the forecast skill when η_B is omitted from Eq. (16), it can be seen that as in Cabanes et al.[2006], the effect of η_B is confined to near the eastern boundaries in the subtropical-to-subpolar North Altantic where the damping $\epsilon > 0$. However, in the tropical-to-subtropical North Atlantic where $\epsilon = 0$, η_B appears to make a larger contribution to the overall skill (roughly 50%) than the other forcing terms in Eq. (16). Further inspection of Fig. 3 and Fig. 4 suggest that this result for the tropical-to-subtropical North Atlantic is due to all the terms in Eq. (16), since, as seen in Fig. 3(b), which shows the forecast skill when η_B is isolated in the model, and Fig. 4(a) and Fig. 4(b), which show the classical wind-driven Rossby wave model with and without eastern boundary forcing, the effect of η_B is confined to the eastern boundaries in the tropical-to-subtropical North Atlantic when the new forcing terms are omitted from Eq. (16).

5. Discussion and conclusion

In this study we have presented and explored a new Rossby wave model of the steric SSH. In the model baroclinic Rossby waves are driven by fluctuations in Ekman pumping, upper ocean mass transport associated with meridional geostrophic thermal wind, upper ocean density content and eastern boundary steric SSH. It is found that the new model captures roughly 60%-100% of the phase and amplitude of observed low frequency steric SSH variations across much of the tropical-to-mid-latitude North Atlantic, with 80%-100% in the tropical-to-subtropical North Atlantic. Furthermore, the new model is a significant improvement on the classical wind-driven Rossby wave model. These results are illustrated in Fig. 2 and Fig. 4, and also Fig. 6 which shows η_S from the new model (red lines) and classical wind-driven Rossby wave model (blue and green lines) superimposed on η_O (black line) at three different locations in the North Atlantic. It can be seen in Fig. 6(a) that η_S from the

new model is almost a perfect match to η_O at this particular location in the tropical-to-subtropical North Atlantic.

The new Rossby wave model and the classical wind-driven Rossby wave model cannot explain low-frequency steric SSH variations in the subpolar North Atlantic. A possible reason for this is that the SSH in the subpolar North Atlantic is dominated by mesoscale eddies, or that other important features are absent from our model. For example, the inertial terms are ignored in our geostrophic ocean circulation model, which are necessary for the parametrization of short Rossby waves (e.g. LaCasce, 2000), and we have also ignored, for example, density variations below the depth of the pycnocline, and variations in the depths of the top and base of the permanent pycnocline. Our results suggest nevertheless that these and other factors do not appear to be important in the entire tropical-to-subtropical North Atlantic, or across much of the subtropical-to-midlatitude North Atlantic.

There are many studies (e.g. Schneider and Miller, 2001) that suggest wind-driven Rossby waves play a role in the low-frequency variability of the steric SSH in the North Pacific. Future work should thus involve investigating Rossby wave steric SSH dynamics in the North Pacific using the new Rossby wave model. Furthermore, Zhang and Wu [2010] showed that North Atlantic sea surface temperature (SST), which partly drives the North Atlantic Oscillation, can be predicted on the basis of SSH variations due to wind-driven baroclinic Rossby waves in some regions of the North Atlantic. We are currently extending their work using the new Rossby wave model.

Finally, there have been many studies that have linked ocean dynamics, in particular the vertical displacement of isopycnals in the deeper ocean, to steric SSH variability (e.g. Hakkinen et al., 2015; Roberts et al., 2017; Polkova, 2015). In particular, Roberts et al. [2017] hypothesize that ocean dynamics plays the dominant role in setting the steric SSH and not local atmospheric forcing. Our results indeed confirm this hypothesis for the tropical-to-subtropical North Atlantic.

Appendix A. Derivation of Eq. (10)

We start by writing the geostrophic and hydrostatic balances below the Ekman layer,

$$-fv = -\frac{1}{\rho_o}\frac{\partial P}{\partial x}, \tag{A.1}$$

$$0 = -\rho g - \frac{\partial P}{\partial z}. \tag{A.2}$$

Integrating Eq. (A.2) vertically from a fixed depth z to the sea surface ($z = \eta_S$), we obtain:

$$P = \int_z^{\eta_S} \rho g \; dz, \tag{A.3}$$

where we have set the atmospheric pressure to zero. Taking the zonal gradient we obtain:

$$\frac{\partial P}{\partial x} = \rho_S g \frac{\partial \eta_S}{\partial x} + \int_z^{\eta_S} g\frac{\partial \rho}{\partial x} \; dz, \tag{A.4}$$

in which ρ_S is the sea surface density. Inserting further into Eq. (A.1) we get:

$$fv = \frac{\rho_S}{\rho_o} g \frac{\partial \eta_S}{\partial x} + \int_z^{\eta_S} g\frac{\partial \rho}{\partial x} \; dz/\rho_o, \tag{A.5}$$

which, after further integration in the vertical from the pycnocline at depth $z = -H_1 - \eta_1$ to just below the Ekman layer leads to:

$$\int_{-H_1-\eta_1}^{-\delta_E} fv \; dz = \frac{\rho_S}{\rho_o} g(H_1 + \eta_1 - \delta_E)\frac{\partial \eta_S}{\partial x} + \int_{-H_1-\eta_1}^{-\delta_E} \left(\int_z^{\eta_S} g\frac{\partial \rho}{\partial x} \; dz'/\rho_o \right) \; dz. \tag{A.6}$$

This can be further developed as:

$$\int_{-H_1-\eta_1}^{-\delta_E} fv \; dz = g(H_1 + \eta_1 - \delta_E)(\frac{\rho_S}{\rho_o}\frac{\partial \eta_S}{\partial x} + \eta_S \frac{\partial \rho_S}{\partial x}) + \int_{-H_1-\eta_1}^{-\delta_E} \left(\int_z^{0} g\frac{\partial \rho}{\partial x} \; dz'/\rho_o \right) \; dz. \tag{A.7}$$

Since the basic state is at rest with no horizontal density gradients, the term proportional to $\eta_S \partial \rho_S/\partial x$ is a second order quantity and $\rho_S/\rho_o \approx 1$. Likewise, for linear perturbations, $\eta_1 \ll H_1$. Assuming further an infinitesimally thin Ekman layer ($\delta_E \to 0$), we finally get:

$$\int_{-H_1-\eta_1}^{-\delta_E} fv \; dz \approx g H_1 \frac{\partial \eta_S}{\partial x} + \int_{-H_1}^{0} \left(\int_z^{0} g\frac{\partial \rho}{\partial x} \; dz'/\rho_o \right) \; dz. \tag{A.8}$$

Multiplication by β/f leads to Eq. (10).

It is important to note that we do not consider the dynamics in the layer below $-H_1-\eta_1$, however, in the 1.5 layer configuration it is necessary to assume that the layer below $-H_1-\eta_1$ is motionless in order to obtain the wind-driven Rossby wave model. This is because in the 1.5 layer model the motionless lower layer assumption leads to a key relation between $\partial\eta_S/\partial t$ and $\partial\eta_1/\partial t$; However, in the derivation of our Rossby wave model we do not need to make any assumptions about the flow in the layer below $-H_1-\eta_1$ to obtain our relation between $\partial\eta_S/\partial t$ and $\partial\eta_1/\partial t$ because it is obtained using the equation for steric sea level in Eq.(1). Note that in our model configuration it can be shown that the layer below $-H_1-\eta_1$ is motionless if horizontal variations in density below this depth are assumed to be negligible.

Appendix B. Analysis of Rossby wave phase speed

As shown in Section 3.2 the Rossby wave phase speed in our model is

$$C_R = -\frac{\hat{g}'\beta H_1}{f^2}, \tag{B.1}$$

where

$$\hat{g}' = g\frac{\hat{\rho}_B-\hat{\rho}_T}{\rho_o}, \tag{B.2}$$

and

$$\hat{\rho}_T = \frac{1}{H_T}\int_{-H_1}^{-H_1+H_T}\hat{\rho}\,dz, \tag{B.3}$$

$$\hat{\rho}_B = \frac{1}{H_B}\int_{-H_1-H_B}^{-H_1}\hat{\rho}\,dz, \tag{B.4}$$

where H_T and H_B are the top and bottom thicknesses of the pycnocline, and $H_2=H_T+H_B$ the total thickness (Fig. 1). Note that since H_T, H_B and H_1 are constant, as in Chelton and Schlax [1996] the shape of C_R is determined from β/f^2, which decreases from the tropics to the poles. In this section

we examine the response of C_R in our model to variations in H_2 with H_1 fixed. Note that $H_2 \to 0$ as $H_T, H_B \to 0$, and $H_2 \to D$ as $H_T \to H_1$ and $H_B \to D - H_1$, where D is the depth of the ocean.

Feucher et al. [2016] attempted to derive estimates for H_2 in the North Atlantic. In the regions where estimates could be obtained, they found that in the tropics $H_2 \approx 50 - 300$m, whereas in the subtropics-to-higher latitudes $H_2 \approx 250 - 700$m; Therefore, H_2 is generally thinner in the tropics than in the subtropics-to-higher latitudes. [Note that they also obtained similar results for H_T and H_B]. It is straightforward to deduce from Eq. (B.3) and Eq. (B.4) that when H_1 is fixed, $\hat{\rho}_T, \hat{\rho}_B \to 0$ as $H_2 \to 0$, and therefore from Eq. (B.2) and Eq. (B.1), $C_R \to 0$; Similarly, it is straightforward to deduce that the maximum C_R is associated with maximum pycnocline thickness $H_2 = D$. Therefore, this analysis along with the work of Feucher et al. [2016] suggests that in observations H_2 plays a key role in determining C_R; In particular, H_2 offsets the effect of β/f^2. Indeed, Fig. B.1 shows C_R in our model when $H_2 = 187$m (dotted curve) and $H_2 = 555$m (broken curve) superimposed on C_R derived by Zhang and Wu [2010] from observations using a 2-D Radon transform. It can be seen that the model C_R is a better match to the observed in the tropics when $H_2 = 187$m, and in the subtropics-to-poles when $H_2 = 555$m. [Note that to compute $\hat{g}'$ we used $\hat{\rho}$ derived from the time and spatially averaged density from ECCO in the model domain used for the integrations, which is described in Appendix C; Furthermore, we set $H_1 = 814$m, and for $H_2 = 187$m we used $H_T = 92$m and $H_B = 95$m to compute $\hat{\rho}_T$ and $\hat{\rho}_B$ yielding $\hat{g}' = 0.005\text{ms}^{-2}$, and similarly for $H_2 = 555$m we used $H_T = 264$m and $H_B = 291$m yielding $\hat{g}' = 0.014\text{ms}^{-2}$].

Appendix C. Solution of the Rossby wave model

Appendix C.1. Model domain

When illustrating the solution to existing Rossby wave models using, for example, wind-stress data from observations, it is only necessary to specify x_E of the model domain, which can be done arbitrarily [e.g. Zhang et al., 2016 (wind-forced); Piecuch and Ponte 2012b (wind and buoyancy forced)]. However, in our Rossby wave model the new forcing terms need to be computed using vertical integrations with

lower limits $-H_1 + H_T$ and $-H_T$ (see the equations defining the forcing terms G_{ρ_t} and G_{ρ_x}). Thus, when using data from observations to derive these terms we need to ensure that at each longitude and latitude of our model domain the ocean topography $D(x, y)$ satisfies $D(x, y) > H_1$, which is not guaranteed if we simply guess x_E [for example $D(x, y) > H_1$ is not likely to be satisfied everywhere near the coasts for all $H_1 = constant$]. Hence, to find the model domain, which includes the eastern and western boundaries, we must first pick a depth for the base of the vertical region, say Z, with $Z > H_1$, and then select all the longitudes and latitudes satisfying $D(x, y) \geq Z$. Note that there is no need to specify the constant ocean depth D from our model framework since we only consider the dynamics in the layer above $-H_1 - \eta_1$.

Appendix C.2. Solution

We obtain the solution to Eq. (12) analytically by integrating along Rossby wave characteristics, $x - C_R t = constant$, from the eastern boundary, x_E, which in our study is written

$$\eta_S \;=\; \eta_B + F_{W_E} + F_{\rho_x} + F_{\rho_t}, \tag{C.1}$$

where

$$\eta_B = \exp\left(\epsilon \frac{x - x_E}{C_R}\right) \eta_S\left(x_E, y, t + \frac{x - x_E}{C_R}\right) \tag{C.2}$$

is the contribution to η_S from the steric SSH at the eastern boundary,

$$\begin{aligned}
F_{W_E} &= \frac{f^2}{g\beta H_1} \int_{x_E}^{x} W_E\left(x', y, t + \frac{x' - x}{C_R}\right) \exp\left(\epsilon \frac{x' - x}{C_R}\right) dx', \\
F_{\rho_x} &= -\frac{1}{H_1 \rho_o} \int_{x_E}^{x} \rho_x\left(x', y, t + \frac{x' - x}{C_R}\right) \exp\left(\epsilon \frac{x' - x}{C_R}\right) dx', \\
F_{\rho_t} &= -\frac{1}{C_R \rho_o} \int_{x_E}^{x} \rho_t\left(x', y, t + \frac{x' - x}{C_R}\right) \exp\left(\epsilon \frac{x' - x}{C_R}\right) dx'
\end{aligned} \tag{C.3}$$

where

$$\rho_x = \int_{-H_1}^{0} [\int_{z}^{0} \frac{\partial \rho}{\partial x}\, dz'] \, dz, \tag{C.4}$$

$$\rho_t = \frac{\partial}{\partial t} \left(\int_{-H_1+H_T}^{0} \rho \, dz \right). \tag{C.5}$$

Note that $\hat{g}'$ does not explicitly appear in our solution but does in the solution to the wind-driven Rossby wave model in the 1.5 layer model used in previous studies (e.g. Zhang et al., 2016).

In Eqs. (C.3-C.5) we set $g = 9.8\text{ms}^{-2}$ and $\rho_o = 1027\text{Kgm}^{-3}$; f is computed from $f = 2\Omega \sin(y)$, where $\Omega = 7.3 \times 10^{-5}\text{rad/s}$; β, W_E, and the derivatives of ρ, are calculated on a cartesian grid using centred differences except near the boundaries or end time points where forward differences are used; from the depths in ECCO we set $H_1 = 814\text{m}$ and $H_T = 180\text{m}$, and we define our model domain such that $D(x, y) \geq -H_1 - H_B = 1007\text{m}$, where $H_B = 193\text{m}$ is the thickness of the lower pycnocline layer. Note that these values of H_1, H_T and H_B have been chosen following Feucher et al. [2016].

The solution is obtained numerically using the Rossby wave phase speeds $C_R(y)$ shown by the black line in Fig. B.1, which is the observed C_R derived by Zhang and Wu [2010] in the North Atlantic. Note that as shown in Appendix B, C_R calculated from our model for different pycnocline thicknesses H_2 can only match the observed C_R at certain latitudes for each H_2.

References

[1] Cababnes, C., Huck, T., Colin de Verdiere, A., 2006. Contributions of wind forcing and surface heating to interannual sea level variations in the Atlantic Ocean. *J. Phys. Oceanogr.* 36, 17391750.

[2] Capotondi, A., Alexander, M.A., 2001. Rossby waves in the tropical North Pacific and their role in decadal thermocline variability. *J. Phys. Oceanogr.* 31, 3496–3515.

[3] Chelton, D.B., Schlax, M.G., 1996. Global observations of oceanic rossby waves. *Science.* 272, 234–238.

[4] Feucher, C., Maze, G., Mercier, H., 2016. Mean Structure of the North Atlantic Subtropical Permanent Pycnocline from In Situ Observations. *J. Atmospheric Ocean.Technol.* 33, 1285–1308. DOI: 10.1175/JTECH–D–15–0192.1.

[5] Forget, G., Campin, J-M., Heimbach, P., Hill, C.N., Ponte, R.M., Wunsch, C., 2016. ECCO version 4: Second Release, http://hdl.handle.net/1721.1/102062.

[6] Fu, L.L., Qiu, B., 2002. Low-frequency variability of the North Pacific Ocean: The roles of boundary- and wind-driven Rossby waves. *J. Geophys. Res.* 107, 3220. DOI:10.1029/ 2001JC001131.

[7] Gill, A.E., 1982. Atmosphere-Ocean Dynamics. *Academic Press, International Geophysics Series* 662.

[8] Hakkinen, S., Rhines, P.B., Worthen, D.L., 2015. Heat content variability in the North Atlantic Ocean in ocean reanalysis. *Geophys.Res.Lett.* 42, 2901–2909. DOI:10.1002/2015GL063299.

[9] Huang, R.X., 2012. Ocean Circulation: Wind-Driven and Thermohaline Processes. *Cambridge University Press.* https://doi.org/10.1017/CBO9780511812293.

[10] LaCasce, J.H., 2000. Baroclinic Rossby waves in a square ocean basin. *J.Phys.Oceanogr.* 30, 3161–3178. DOI:10.1175/ 1520–0485(2000)030,3161:BRWIAS.2.0.CO;2.

[11] Lacasce, J.H., Pedlosky, J., 2004. The instability of Rossby basin modes and the oceanic eddy field. *J.Phys.Oceanogr.* 34, 2027–2041.

[12] Liang, X., Piecuch, C.G., Ponte, R.M., Forget, G., Wunsch, C., Heimbach, P., 2017. Change of the Global Ocean Vertical Heat Transport over 1993-2010. *J.Climate.* 30(14), 5319–5327.

[13] M.Calafat, F.M., Wahl, T., Lindsten, F., Williams, J., Frajka-Williams, E., 2018. Coherent modulation of the sea-level annual cycle in the United States by Atlantic Rossby waves. *Nat. Commun.* 9 (1). DOI: 10.1038/s41467-018-04898-y.

[14] Piecuch, C. G., Ponte, R.M., 2011. Mechanisms of interannual steric sea level variability. *Geophys. Res. Lett.* 38, L15605. DOI:10.1029/2011GL048440.

[15] Piecuch, C. G., Ponte, R.M., 2012a. Buoyancy-driven interannual sea level changes in the southeast tropical Pacific. *Geophys. Res. Lett.* 39. https:/doi.org/10.1029/2012GL051130.

[16] Piecuch, C. G., Ponte, R.M., 2012b. Buoyancy-Driven Interannual Sea Level Changes in the Tropical South Atlantic. *J. Phys. Oceanogr.* 43, 533–547.

[17] Polkova, I., Köhl, A., Stammer, D., 2015. Predictive skill for regional interannual steric sea level and mechanisms for predictability. *J. Climate.* 28, 7407–7419. DOI:10.1175/JCLI–D–14–00811.1.

[18] Qiu, B., Chen, S., 2006. Decadal variability in the large-scale sea surface height field of the South Pacific Ocean: Observations and cause. *J. Phys. Oceanogr.* 36, 1751–1762. DOI:10.1175/JPO2943.1.

[19] Roberts, C.D., Palmer, R.P., Allan, R.P., Desbruyeres, D.G., Hyder, P., Liu, C., Smith, D., 2017. Surface flux and ocean heat transport convergence contributions to seasonal and interannual variations of ocean heat content. *J.Geophys.Res.Oceans.* 122, 726–744. DOI:10.1002/206JC012278.

[20] Schneider, N., Miller, A. J., 2001. Predicting western North Pacific Ocean climate. *J. Climate.* 14, 3997–4002.

[21] Sturges, W., Hong, B., Clarke, A.J., 1998. Decadal wind forcing of the North Atlantic subtropical gyre. *J. Phys. Oceanogr.* 28, 659–668. DOI:10.1175/1520–0485(1998)028,0659:DWFOTN.2.0.CO;2.

[22] Wunsch, C., Heimbach, P., 2007. Practical global oceanic state estimate. *Physica D.* 230, 197–208.

[23] Zhang, J., Kelly, K.A., Thompson, L.A., 2016. The role of heating, winds, and topography on sea level changes in the North Atlantic. *J. Geophys. Res. Oceans.* 121, 2887–2900. DOI:10.1002/2015JC011492.

[24] Zhang, H., Wu, L., 2010. Predicting North Atlantic sea surface temperature variability on the basis of the first-mode baroclinic Rossby wave model. *J. Geophys. Res.* 115. C09030. DOI: 10.1029/2009JC006017.

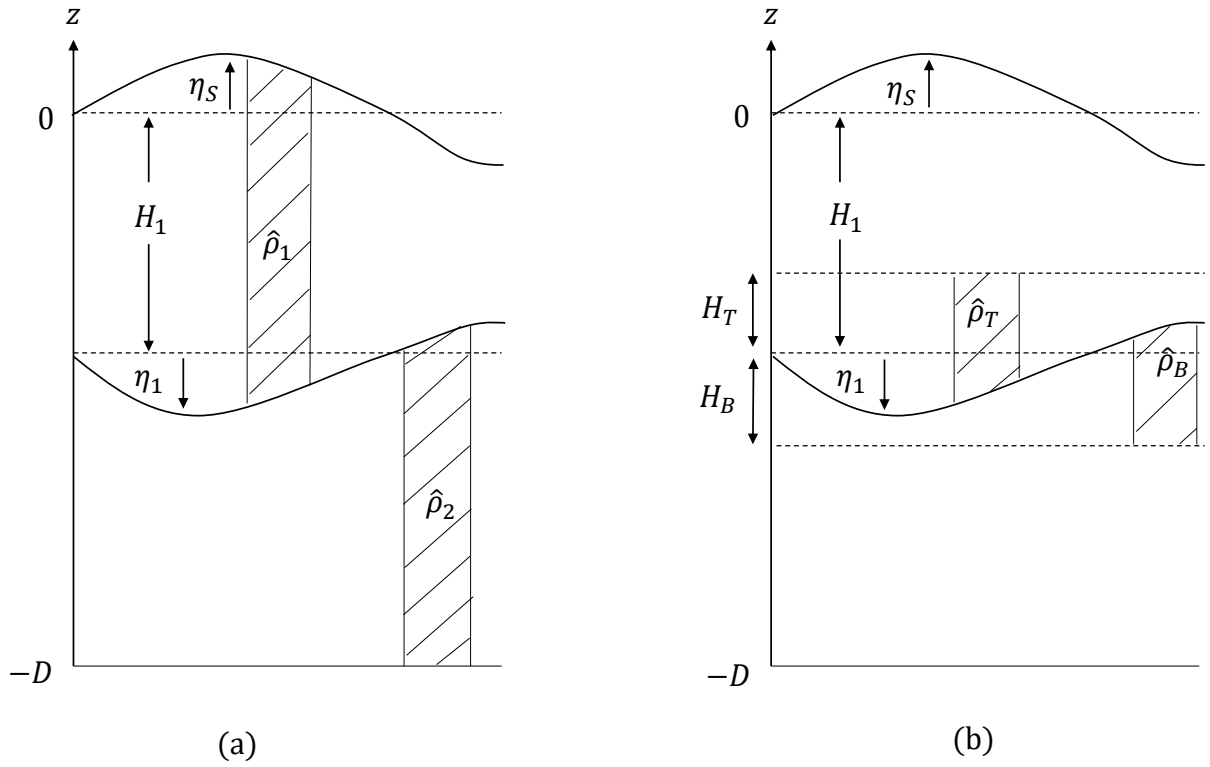

Fig. 1: Model Framework (a) standard two-layer model (b) the new model. The hatched columns help to visualize the portion of the fluid column whose average density is assumed to be constant.

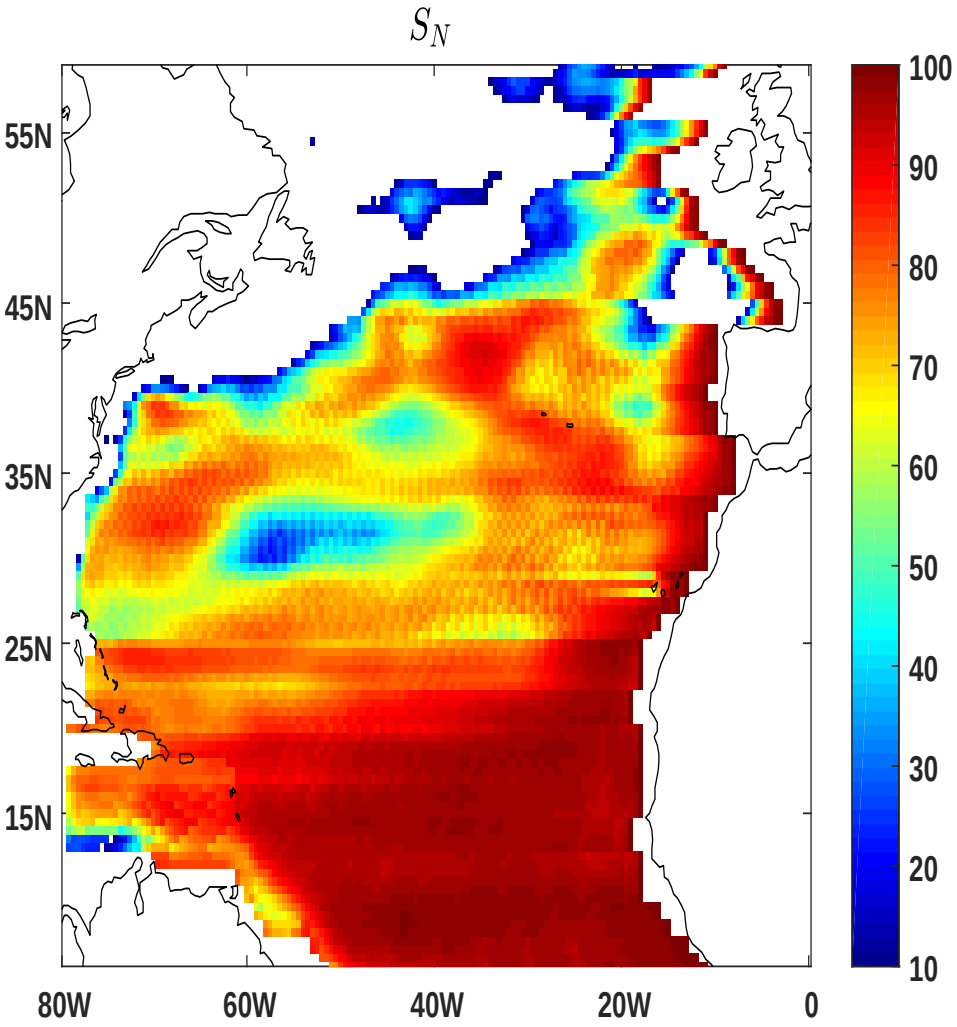

Fig. 2: Forecast skill, S_N, for new Rossby wave model.

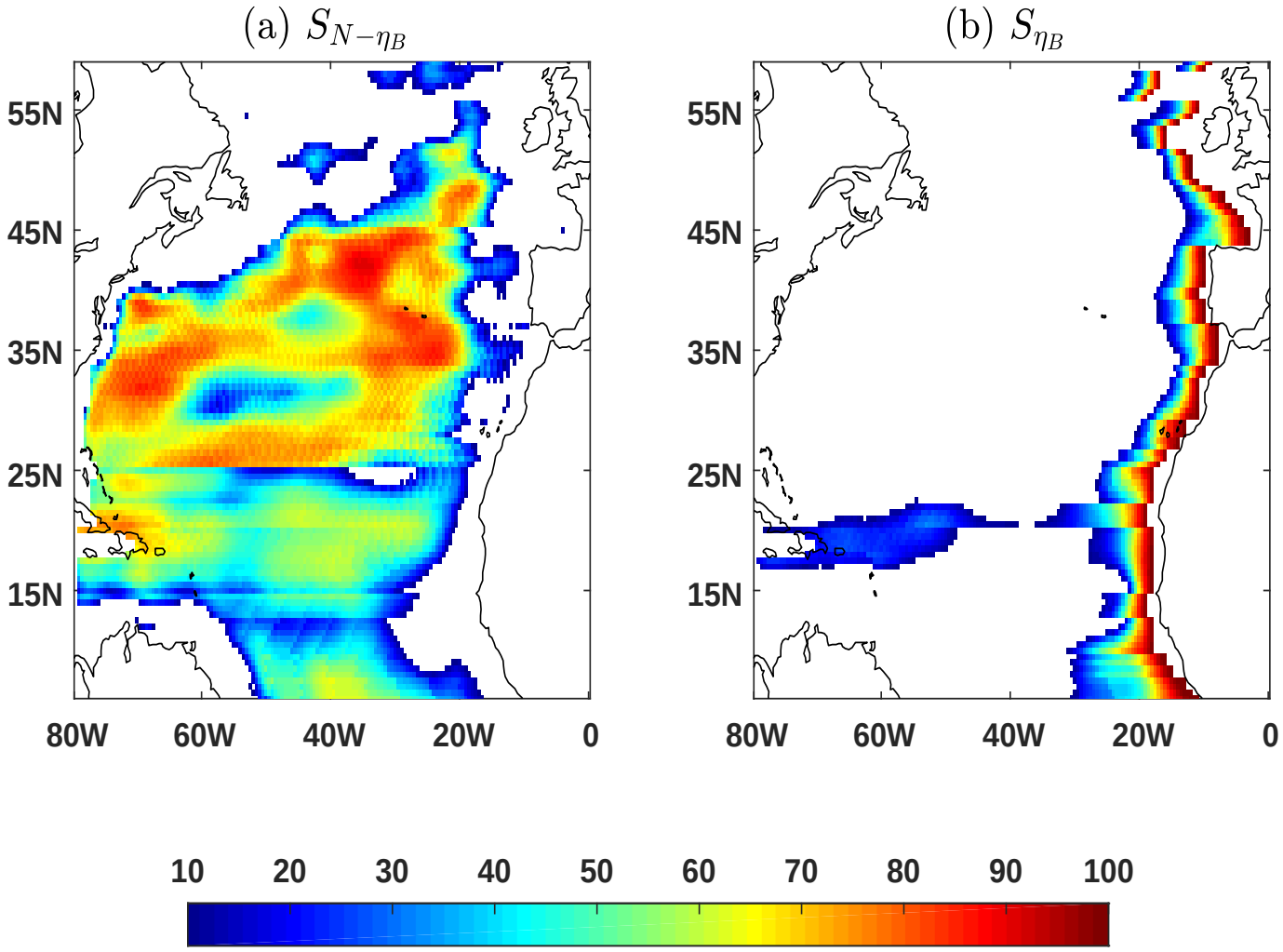

Fig. 3: (a) shows forecast skill, $S_{N-\eta_B}$, when η_B is omitted from the new model. (b) shows forecast skill, S_{η_B}, when η_B is isolated in the model.

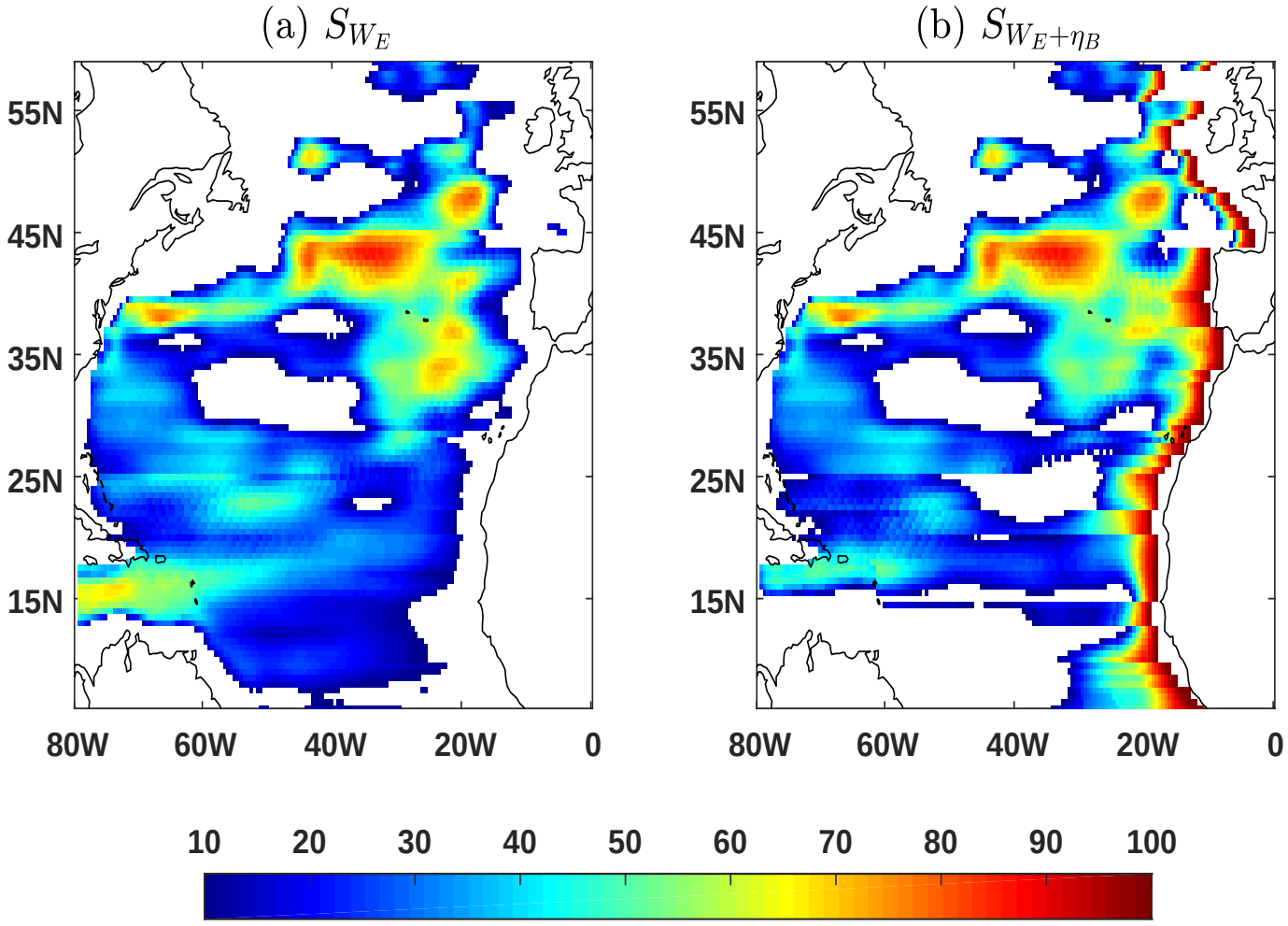

Fig. 4: (a) shows forecast skill, S_{W_E}, when W_E is isolated in the model. (b) shows forecast skill, $S_{W_E+\eta_B}$, when solution is determined by W_E and η_B.

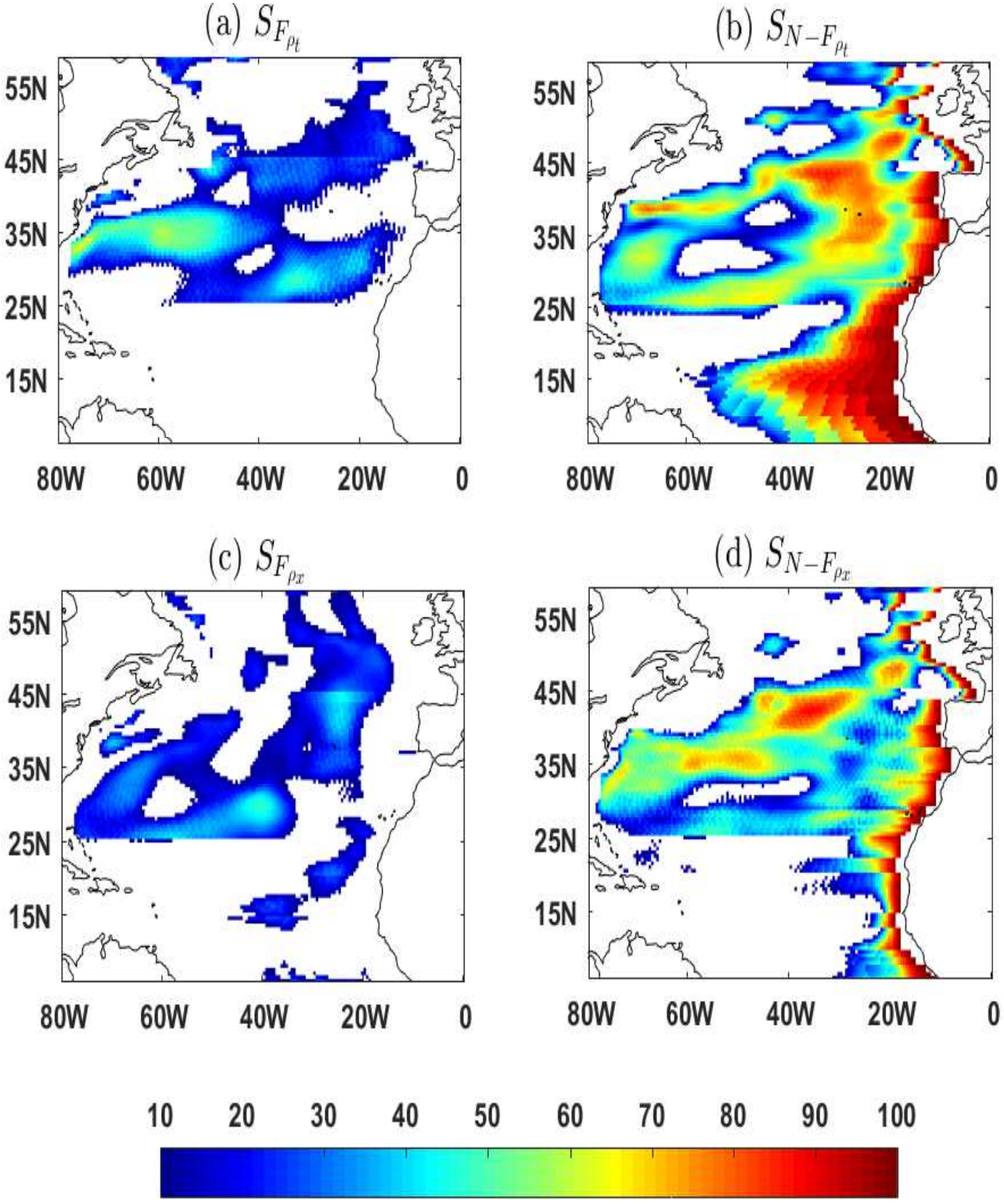

Fig. 5: (a) shows forecast skill, S_{ρ_t}, when F_{ρ_t} is isolated in the model, and (b) shows forecast skill, $S_{F-F_{\rho_t}}$, when F_{ρ_t} is omitted from the full model. (c) and (d) show the same as (a) and (b) but for F_{ρ_x}.

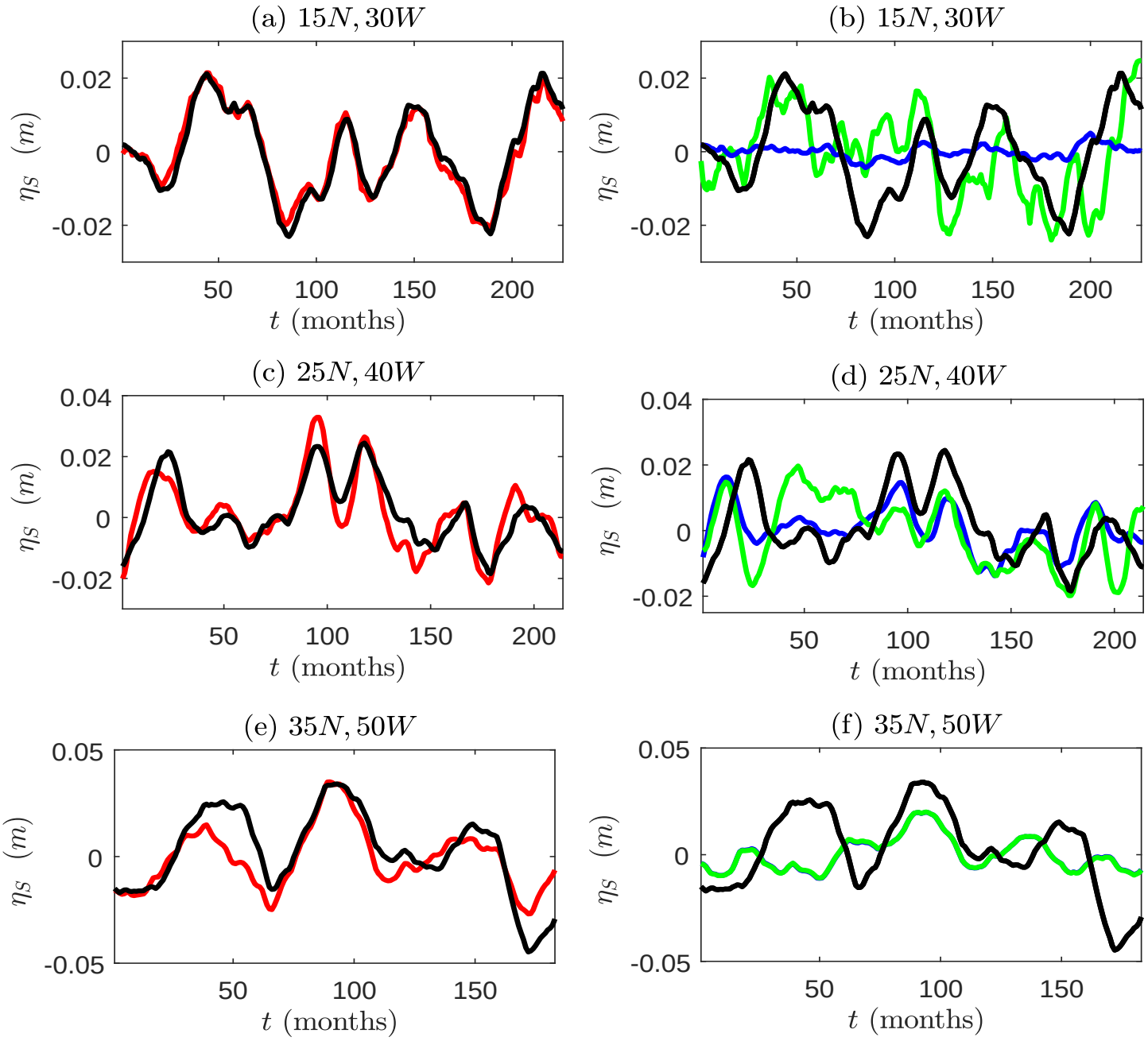

Fig. 6: Time series of observed and model simulated SSH anomalies. (a) and (b) are taken at $15N, 30W$; (c) and (d) at $25N, 40W$; and (e) and (f) at $35N, 50W$. Note that the length of each time series differs because of the different Rossby wave transit times. In each panel the black lines are the observed steric SSH. In (a), (c) and (e) the red lines are model simulated SSH from the new Rossby wave model; and in (b), (d) and (f) the green lines are the model simulated SSH from the classical wind-driven Rossby wave model with eastern boundary SSH anomalies, and the blue lines are the model simulated SSH from the wind-driven model but with no eastern boundary SSH anomalies. Note that in (f) the blue curve is not visible as it is essentially identical to the green curve.

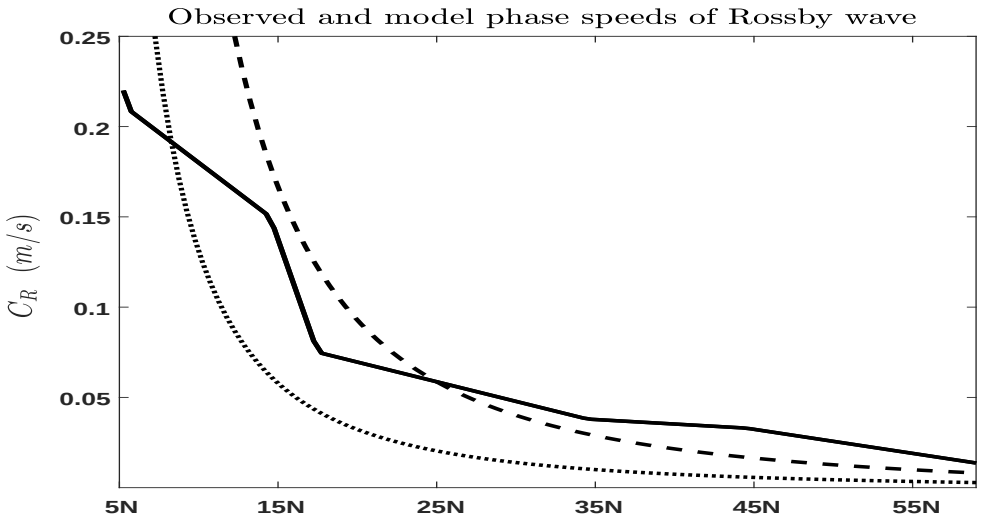

Fig. B.1: Rossby wave phase speeds, C_R: thick black line is C_R taken from Zhang and Wu [2010], and the broken and dotted lines are C_R predicted by the model when the basic state thickness of the permanent pycnocline is $H_2 = 555$m and $H_2 = 187$m respectively.